



Synthesis and electrochemical properties of cubic-like ZnMoO₄ anode materials

Qingyun Ma¹, Xuetian Li¹, Guangyu Li¹, and Zhongcai Shao^{1,*} 

¹ School of Environmental and Chemical Engineering, Shenyang Ligong University, Shenyang, Liaoning Province, People's Republic of China

Received: 16 April 2020

Accepted: 13 June 2020

Published online:

25 June 2020

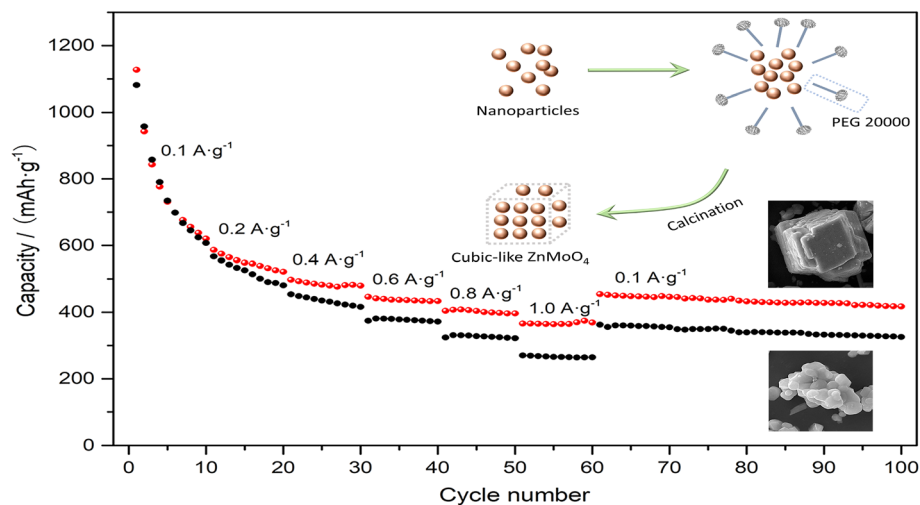
© Springer Science+Business Media, LLC, part of Springer Nature 2020

ABSTRACT

We prepared cubic-like ZnMoO₄ anode material via precipitation-freeze drying method and calcining directly in the air using zinc acetate and ammonium molybdate tetrahydrate as raw materials. Through various characterization methods, the structure, morphology and electrochemical properties of cubic-like ZnMoO₄ were studied. By comparing the structure and morphology of cubic-like ZnMoO₄ and ordinary ZnMoO₄, cubic-like ZnMoO₄ had a smaller particle size and good dispersibility. In addition, compared with ordinary ZnMoO₄, the electrochemical performance of cubic-like ZnMoO₄ was improved. When accepted as an anode material for lithium-ion secondary batteries, the cubic-like ZnMoO₄ provided a discharge capacity of 457.7 mAh g⁻¹ at a current density of 0.1 A g⁻¹ after 100 cycles. Moreover, it exhibited excellent electrochemical properties even at high current densities. The electrochemical results indicated that the cubic-like ZnMoO₄ has high capacity, good rate ability, and outstanding cycle stability.

Address correspondence to E-mail: 840865127@qq.com

GRAPHIC ABSTRACT



Introduction

Lithium-ion battery (LIB) is a widely used primary energy battery [1–4]. It develops rapidly and occupies a great position in the energy market. The anode material is an important part of the LIB. Graphite has the advantages of low-priced, large storage capacity and good electrical conductivity, which be supposed to be a commonly used industrial anode material [5–7]. However, the theoretical capacity of this anode material is relatively low at 372 mAh g^{-1} [8], which places restrictions on its application in high energy density batteries. The development of new anode material capable of providing high discharge capacity has become a key to break through the restrictions of LIB extensive application.

The molybdate is considered to be a promising and considerable anode material [9], because of the high valence state of molybdenum, rich resources, and low price. Recently, these MMoO_4 combinations include CoMoO_4 [10, 11], FeMoO_4 [12], MnMoO_4 [13–15], NiMoO_4 [16, 17], and ZnMoO_4 [18, 19]. However, MMoO_4 anode material has the disadvantage of poor cycle stability during the lithiation/delithiation process [20], which limits their widespread application. According to previously reported studies, materials with certain special morphologies have good cycle

stability and excellent rate performance, such as single crystals [21, 22], nanorods [23, 24], and nanosheets [25].

Among molybdates, molybdenum zinc oxide (ZnMoO_4) as a unique semiconductor material is considered to be one of the most potent alternative materials for high energy density LIB, with a significant theoretical capacity of 951.6 mAh g^{-1} [26]. In this work, polyethylene glycol (PEG) 20,000 was used as a surfactant, and cubic-like ZnMoO_4 (ZMO-C) material was synthesized by precipitation-freeze drying method. It is found that the addition of surfactants could effectively avoid the agglomeration of materials. The structure, surface morphology, and electrochemical performance of the ZMO-C were researched.

Experimental section

Material preparation

The raw materials are polyethylene glycol 20,000 ($\text{HO}(\text{CH}_2\text{CH}_2\text{O})_n\text{H}$, AR) zinc acetate ($\text{C}_4\text{H}_6\text{O}_4 \cdot \text{Zn} \cdot 2\text{H}_2\text{O}$, AR) and ammonium molybdate tetrahydrate ($(\text{NH}_4)_6\text{Mo}_7\text{O}_{24} \cdot 4\text{H}_2\text{O}$, AR).

PEG 20,000 (1 wt% of gross weight) and $(\text{NH}_4)_6\text{Mo}_7\text{O}_{24}\cdot 4\text{H}_2\text{O}$ (1 mmol) were dissolved in the deionized water. With vigorous stirring, $\text{C}_4\text{H}_6\text{O}_4\cdot \text{Zn}\cdot 2\text{H}_2\text{O}$ (7 mmol) was added to the above solution. The resulting mixture was freeze-dried in a vacuum freeze-drying oven. Finally, the precursor was placed in a muffle furnace in the air environment and calcined at 600 °C for 5 h to obtain ZMO-C. At the same time, ZnMoO_4 (ZMO) was also prepared without PEG 20,000 for comparison purposes.

Structural characterization and electrochemical tests

The crystallinity of the materials was characterized by an X-ray diffractometer (XRD, BDX3300) with $\text{Cu-K}\alpha$ radiation in the range of 15°–50° at a scan rate of 2°·min⁻¹. Information on the surface morphology of the samples was obtained using a tungsten scanning electron microscope (SEM, Vega3-xmu).

The working electrodes were primed by blending the active materials, acetylene black, and polyvinylidene fluoride (PVDF as a binder) in a weight ratio of 8:1:1 in N-methyl-2-pyrrolidone (NMP) solution. The electrochemical properties were studied in CR 2032 button cells. The lithium metal sheets were applied as the counter electrodes and 1 M LiPF_6 in ethyl carbonate (EC), ethyl methyl carbonate (EMC) and dimethyl carbonate (DMC, EC: EMC: DMC = 1:1:1 vol%) as the electrolyte. The diameter of each electrode plate was 14 mm. The weight of the active material on the electrode plate was about 1.8 mg. The button cells are produced in an argon-filled glove box. The charge–discharge investigation of cells was realized in the range of 0.01 to 3.00 V in the battery test system (Neware Co., Ltd., China). The electrochemical impedance (EIS) measurements were accomplished at the CHI660E electrochemical workstation in the range of 10⁵ to 10⁻¹ Hz. The cyclic voltammetry (CV) measurements were made at a scanning rate of 0.1 mV·s⁻¹ in the range of 0–3.00 V using the CHI660E electrochemical workstation. All measurements were made at room temperature.

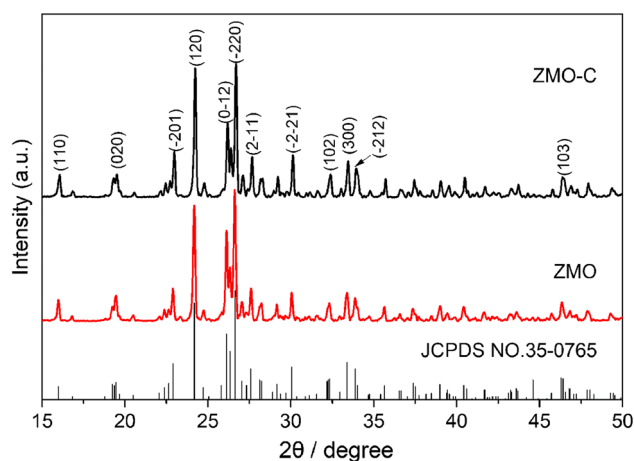


Figure 1 XRD patterns of ZMO-C and ZMO.

Results and discussion

XRD test analysis of materials

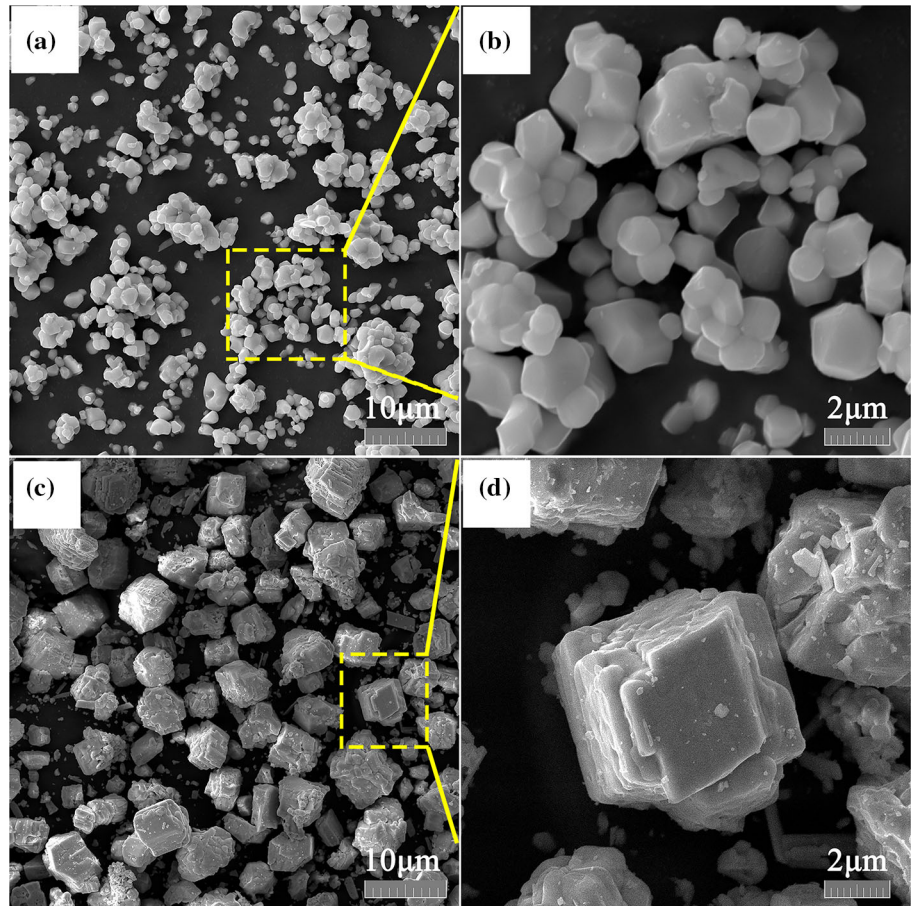
The purity and crystallographic structure of the samples are tested by XRD. As illustrated in Fig. 1, diffraction peaks of the two samples are related to $\alpha\text{-ZnMoO}_4$ (JCPDS NO. 35–0765), and almost no diffraction peaks of other phases are observed in the pattern, which confirmed the high purity of the sample. The detailed parameters calculated by XRD are shown in Table 1. Compared with ZMO, the average particle size ($D = \frac{k\lambda}{B\cos\theta}$) [27] of ZMO-C is smaller, which may due to the coating effect of PEG 20,000, the growth of a single particle is restricted.

Morphological test and analysis of materials

Figure 2 shows SEM images of ZMO and ZMO-C. ZMO is an irregular block with a size mainly around 1.0–2.0 μm . Besides, obvious agglomeration can be observed. It can be seen from the graphs of different magnifications that ZMO-C has a compact cubic-like morphology with obvious layering. On the one hand, the cubic layered structure is conducive to buffer volume expansion and stable structure during charging and discharging. On the other hand, the cubic layered structure can broaden the diffusion path and shorten the diffusion channel of Li^+ . Compared with ZMO, the agglomeration of ZMO-C is significantly reduced. This is because after adding PEG 20,000 in the precipitation process, the particles are covered by the surfactant molecules to reduce the contact between the particles so that the particles are

Table 1 Lattice parameters of ZMO-C and ZMO, respectively

Samples	<i>a</i> (Å)	<i>b</i> (Å)	<i>c</i> (Å)	α (°)	β (°)	γ (°)	<i>D</i> (nm)
ZMO-C	8.36456 (0.00398)	9.68985 (0.00421)	6.96022 (0.03467)	106.859 (0.00897)	101.761 (0.02025)	96.755 (0.02556)	69 (1.9)
ZMO	8.36967 (0.00335)	9.69428 (0.00385)	6.96335 (0.00300)	106.865 (0.03548)	101.765 (0.08177)	96.773 (0.13579)	77 (2.1)

Figure 2 SEM images of ZMO (a, b) and ZMO-C (c, d).

in a uniform dispersion state. It is generally believed that good dispersion can effectively improve the cyclic stability of materials [28].

Charge and discharge test of materials

The initial charge–discharge curves and cycle abilities of ZMO and ZMO-C at 0.1 A g⁻¹ are revealed in Fig. 3a, b. The initial discharge capacity of ZMO is 1115.8 mAh g⁻¹. Compared with ZMO, ZMO-C has a higher initial discharge capacity of 1133.2 mAh g⁻¹. During the initial discharge, the formation of a solid electrolyte interface (SEI) film consumes a large

amount of Li to provide a capacity contribution, so the first discharge capacities of ZMO and ZMO-C are both higher than the theoretical capacity of ZnMoO₄ (951.6 mAh g⁻¹) [26, 29]. After 100 cycles, the discharge capacities of ZMO and ZMO-C are 392.3 and 457.7 mAh g⁻¹. The capacity retention rates are 35.2% and 40.4%, respectively. The results show that ZMO-C has higher discharge capacity and cycle performance.

Figure 3c, d show the initial charge–discharge curves and cycle abilities of ZMO and ZMO-C at 1.0 A g⁻¹. Due to the rapid insertion of Li⁺ at high

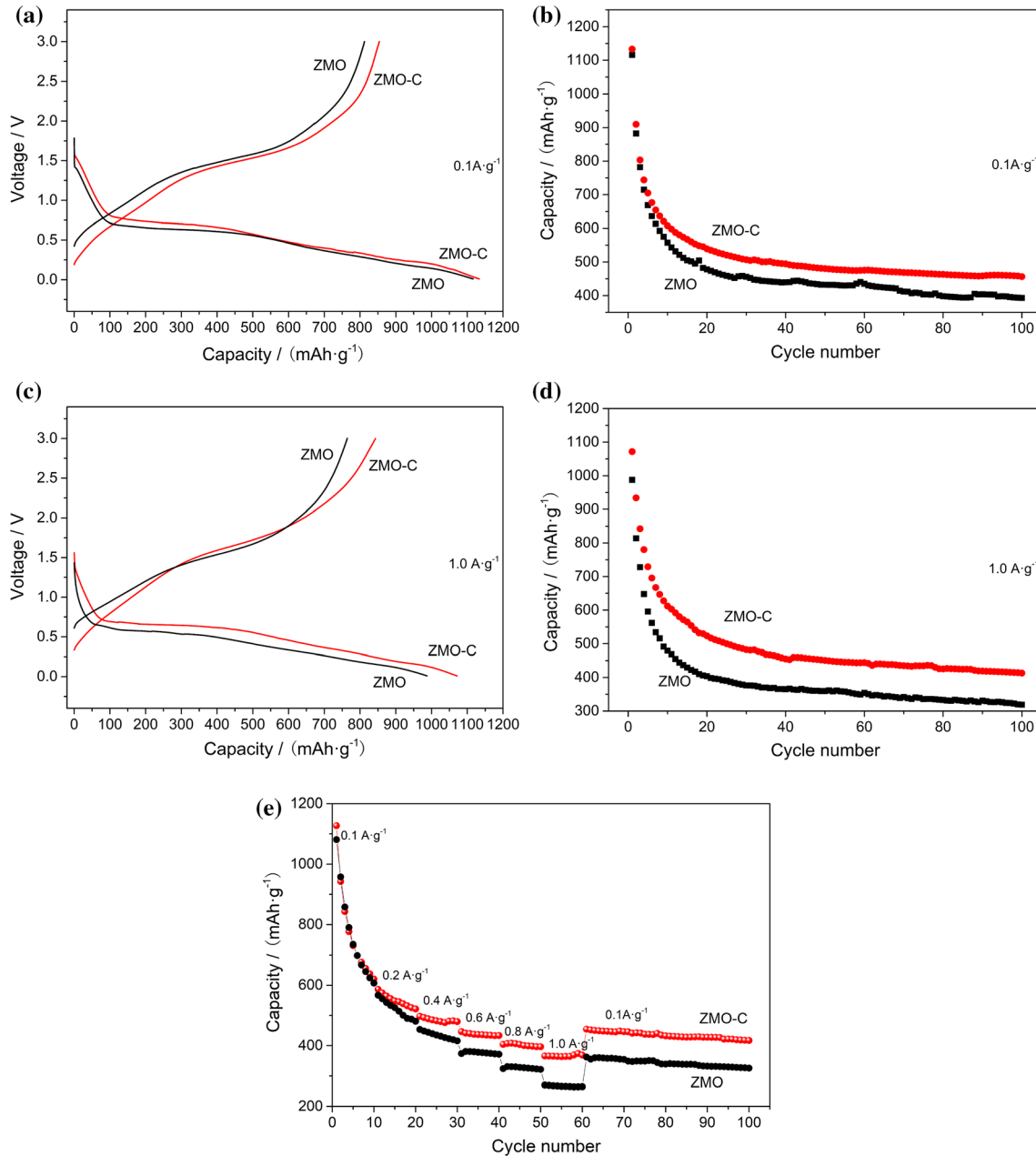


Figure 3 Electrochemical performance of ZMO-C and ZMO. **a** Initial charge/discharge curves at 0.1 A g⁻¹. **b** Cycling performance. **c** Initial charge/discharge curves at 1.0 A g⁻¹. **d** Cycling performance. **e** Rate capabilities at different current densities.

current density, the discharge capacity of both materials decreases with increasing current density. However, compared with ZMO, ZMO-C shows a larger discharge capacity (413.0 mAh g⁻¹), which means that with the rate increases, the anti-polarization capability of ZMO-C is stronger. It can be found that when the current density increases to 1.0 A g⁻¹, the specific capacities of Fig. 3a, b are close to Fig. 3c, d. On the one hand, due to the constant current charging and discharging at low current density, the

electrolyte cannot fully penetrate the active material, resulting in only a part of the active material being fully penetrated [30]. On the other hand, the small change in discharge capacity when the current density increases are also related to the high crystallinity of ZMO-C. The high crystallinity can effectively avoid the destruction of the crystal structure of the material under the high current impact, maintaining a stable discharge capacity.

Table 2 Rate performances of ZMO and ZMO-C at various current densities

Samples	Discharge capability (mAh g ⁻¹)					
	0.1 A g ⁻¹	0.2 A g ⁻¹	0.4 A g ⁻¹	0.6 A g ⁻¹	0.8 A g ⁻¹	1.0 A g ⁻¹
ZMO	607.3	480.9	416.1	371.8	321.8	264.7
ZMO-C	620.6	521.7	479.9	433.7	396.4	369.1

Rate performance is an important factor for practical battery applications. Figure 3e shows the rate performance for ZMO and ZMO-C electrodes. The detailed results of ZMO and ZMO-C are listed in Table 2. Even to the current density rebounds to 0.1 A g⁻¹, the ZMO-C electrode still exhibits a higher discharge capacity than the ZMO electrode in subsequent cycles, which indicates that the ZMO-C electrode has better reversibility and stability.

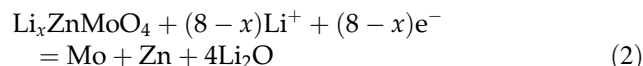
It can be seen from Fig. 3a, c that all electrodes exhibit similar Li⁺ insertion tendency during the initial discharge, indicating that the difference in material structure and morphology does not affect the electrochemical behavior of the conversion reaction during the initial lithium storage [31]. However, the capacity of ZMO-C is higher than that of ZMO after cycling. The results of the charge and discharge test show that the discharge capacity and reversibility of ZMO-C are significantly better than ZMO. It may attribute to the small average particle size and unique cubic layered structure of ZMO-C leading to faster lithium diffusion in the electrode.

Cyclic voltammetry (CV) test and analysis of materials

The original three successive cyclic voltammetry (CV) curves of ZMO-C at 0.1 mV·s⁻¹ is shown in Fig. 4a. Some differences between the three curves can be

observed in the potential range of 0.01–3.00 V. A broad peak at 0.62 V can be detected in the first cathode scan curve, which can be chalked up to the formation of the SEI film [19]. The two peaks at 1.51 and 0.25 V are due to the reaction of Zn²⁺ to Zn⁰ and Mo⁶⁺ to Mo⁰ and lithification of zinc particles to form LiZn alloys [32]. In the primary anode scan curve, the two peaks of 0.82 and 1.54 V conform to the lithium extraction step of LiZn alloy and the oxidation of the metal to metal ion (Mo⁰/Mo⁶⁺ and Zn⁰/Zn²⁺).

During the first discharge, Li is inserted into the octahedron [ZnO₆] and tetrahedron [MoO₄] [33] to form Li_xZnMoO₄, and gradually formed Zn particles and Mo particles. The zinc particles further react with lithium ions to form a LiZn alloy in the next step. As shown in the following equation.



During the charging stage, the zinc particles and Mo particles obtained after LiZn de-alloying react with Li₂O to generate ZnO and MoO₃, respectively.

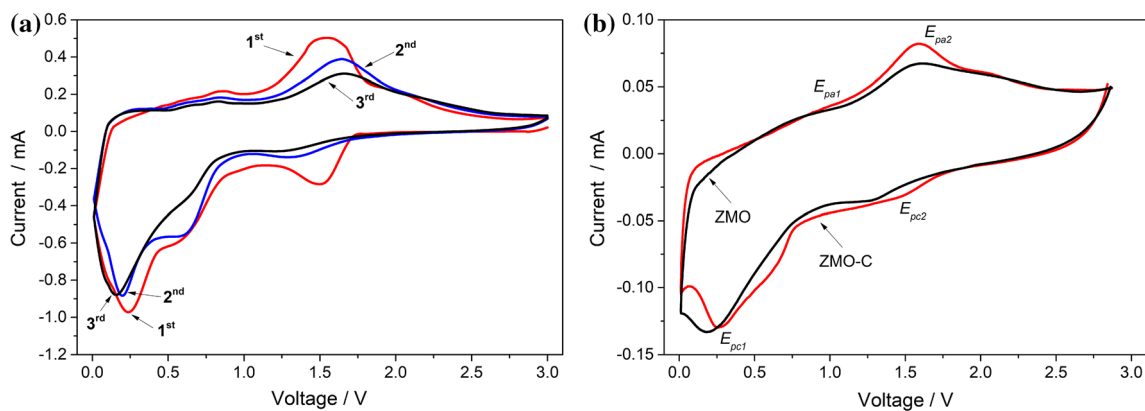
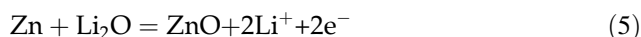
**Figure 4** CV curves at a scan rate of 0.1 mV·s⁻¹. **a** Initial three consecutive of ZMO-C **b** ZMO-C and ZMO at 0.1 A g⁻¹ after 50 cycles.

Table 3 Peak parameters of CV curves for ZMO and ZMO-C; ΔE_p is the separation between E_{pa} and E_{pc} .

Samples	$E_{pa1}(V)$	$E_{pa2}(V)$	$E_{pc1}(V)$	$E_{pc2}(V)$	$\Delta E_{p1}(mV)$	$\Delta E_{p2}(mV)$
ZMO	0.814	1.597	0.17	1.264	644	333
ZMO-C	0.845	1.591	0.255	1.427	590	164



In the subsequent CV curve, the position of the reduction peak shifted slightly, which may be due to the change in the microstructure of the active material [34]. It can be found that the second and the third CV curve have a high overlapping rate, indicating that the synthesized ZMO-C electrode still maintains a steady crystal structure and reversible electrochemical performance [35].

Figure 4b exhibits the CV curves of ZMO-C and ZMO at 0.1 A g^{-1} after 50 cycles. The peak parameters of the CV curve of ZMO-C and ZMO are shown in Table 3. Compared with ZMO, the ΔE_p of ZMO-C is smaller, which indicates that the intercalation-delamination process of Li^+ is faster and the shorter diffusion path of Li^+ [36].

The electrochemical impedance spectrum (EIS) test analysis of materials

To further research the significance of the cubic-like structure on the electrochemical impedance spectrum (EIS), EIS measurements are performed on the battery. The Nyquist plots consist of two parts, including semicircles and diagonal lines. The semicircle from high-frequency to intermediate-frequency is associated with the charge transfer resistance (R_{ct}) in the electrolyte and electrode interface. Li^+ diffusion appears as an oblique line in the low-frequency region [37].

It is worth noting that the two electrodes after circulation have lower charge transfer resistance, which is due to the Li^+ path is fully activated during the cycle. The diameter of the semicircle of the ZMO-C electrode is more cramped than the diameter of the semicircle of the ZMO, which can be further confirmed by the equivalent circuit (inserted in Fig. 5a). The equivalent circuit is composed of ohmic resistance (R_s), charge transfer resistance (R_{ct}), constant-phase element (CPE), and Warburg impedance (W_O) [38]. Table 4 lists the corresponding data.

As shown, the R_{ct} of ZMO-C is significantly smaller than that of ZMO, which indicates that the reaction kinetics of ZMO-C with a cubic-like structure is improved. Besides, the lithium-ion diffusion coefficient (D_{Li}) of the electrode can be obtained by Eq. 7:

$$D_{\text{Li}} = R^2 T^2 / (2A^2 n^4 F^4 C^2 s^2) \quad (7)$$

In the formula, R is a gas constant, T is an absolute temperature, A is an electrode surface area, n is the number of transferred electrons, F is a Faraday constant, C is a lithium-ion concentration, and σ is a Warburg impedance coefficient. σ is the slope of line $Z' \sim \omega^{-1/2}$ obtained from Fig. 5b. Compared to ZMO, lithium-ion transfer and diffusion in ZMO-C materials are faster. This may be due to the small particle size and unique structure of ZMO-C, which accelerates lithium ion transfer.

The exchange current (j^0) represents the reversibility of the electrode reaction [39] and can be obtained from Eq. (8).

$$j^0 = RT/nFR_{ct} \quad (8)$$

In the formula, R is the gas constant, T is the absolute temperature, n is charge transfer number and F is the Faraday constant.

The exchange current of ZMO-C is larger than that of ZMO, which indicates that the reversibility of the electrode reaction of ZMO-C is higher than ZMO. This is considered to be the reason why ZMO-C has a better electrochemical performance.

The influence of the material SEI film formation process can be inferred by the change of the Bode plots in the middle and high-frequency regions. The frequency range corresponding to the SEI film formation process of the anode material is mainly concentrated in 10–1000 Hz [40]. As the frequency increases, the impedance value decreases (Fig. 5c), which is the result of the Li^+ path is gradually activated during the cycle. The impedance decreases slowly in the range of 10–1000 Hz, indicating that this area is the interface between the passivation layer and the anode surface. Comparing respectively the phase angle changes of the two electrodes before and after the cycle in the range of 10–1000 Hz (Fig. 5d), it

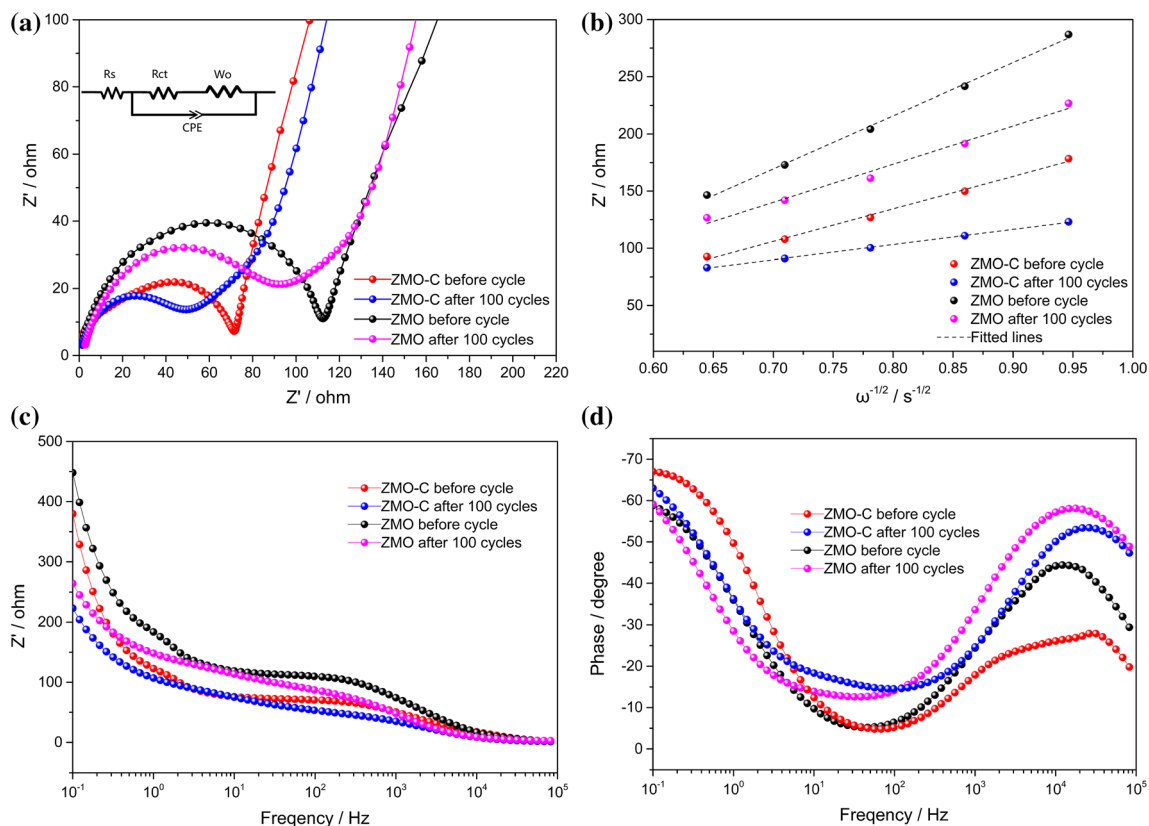


Figure 5 **a** Nyquist plots and equivalent circuit of ZMO and ZMO-C. **b** The linear relationship of Z'' as a function of the square root of frequency ($\omega^{-1/2}$) in the low-frequency region. **c** Bode magnitude on a logarithmic scale and **d** phase angle.

Table 4 The results of EIS, the diffusion of lithium-ion coefficients (D_{Li}) and the exchange current density (j^0) of ZMO and ZMO-C, respectively

Samples	R_s (Ω)	R_{ct} (Ω)	σ	D_{Li} ($\text{cm}^2 \cdot \text{s}^{-1}$)	j^0 ($\text{A} \cdot \text{cm}^{-2}$)
ZMO Before cycle	1.96	112.40	464.77	7.3×10^{-20}	2.5×10^{-5}
ZMO After 100 cycles	2.77	93.39	334.23	1.4×10^{-19}	3.1×10^{-5}
ZMO-C Before cycle	1.32	71.41	284.67	1.9×10^{-19}	4.0×10^{-5}
ZMO-C After 100 cycles	1.36	49.38	132.35	9.0×10^{-19}	5.8×10^{-5}

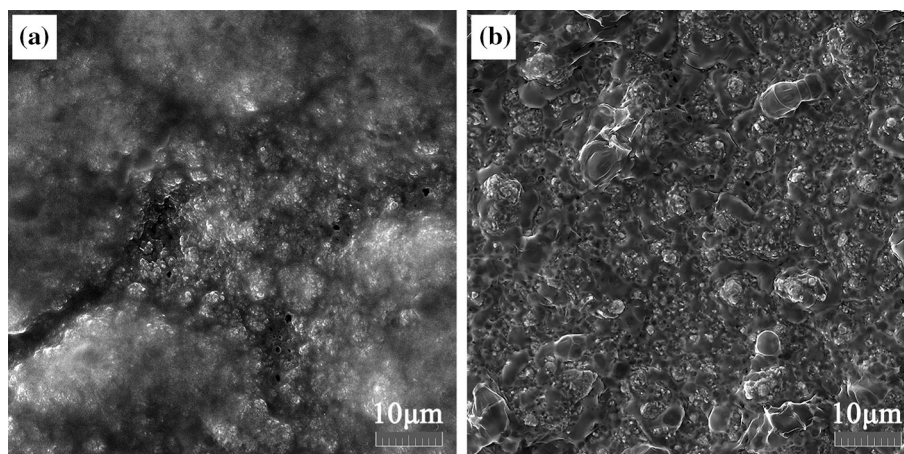
can be found that ZMO-C has a slower trend than ZMO, proving that the passivation layer in ZMO-C electrode surface is more evenly distributed [41]. It is mutually corroborated with the superior dynamics and polarization of the ZMO-C obtained from the Nyquist plots.

Morphological test and analysis of the electrodes after cycling

To further understand the reason for the performance improvement caused by the morphological change of

ZnMoO_4 , the microscopic morphology of the two samples after cycling was observed. It can be observed from Fig. 6a that the ZMO electrode has a significant volume expansion phenomenon. In contrast, although the ZMO-C electrode has a small portion of protrusions, it maintains a flat surface structure (Fig. 6 b). It shows that the cubic morphology material can effectively relieve the volume expansion of the material to a certain extent during the cycling process. Therefore, it is believed that excellent cycle stability and rate performance of

Figure 6 SEM images of **a** ZMO electrode and **b** ZMO-C electrode after 100 cycles at 1.0 A g^{-1} .



ZMO-C can be attributed to its minimal volume change and structural stability [42].

Conclusions

In summary, we successfully prepared cubic-like ZnMoO_4 by precipitation-freeze drying method using PEG 20,000 as a surfactant. XRD analysis shows that the pure phase of ZMO-C is free of impurities, and ZMO-C has a smaller average particle size than ZMO. SEM analysis shows that ZMO-C has a cubic shape and is uniformly dispersed. The charge and discharge test results show that compared with ZMO, ZMO-C has higher discharge capacity and better cycle performance. The charge and discharge mechanism of ZMO-C is analyzed by CV, and ZMO-C had higher reactivity. The EIS results show that the diffusion coefficient of ZMO-C is larger than ZMO, further indicating that ZMO-C has a superior electrochemical performance.

Acknowledgements

The authors gratefully acknowledge supports by the Natural Science Foundation of Liaoning Province (No. 2020-BS-154).

Compliance with ethical standards

Conflict of interest The authors report no conflicts of interest associated with this publication.

References

- [1] Gao W, Zhang X, Zheng X, Lin X, Cao H, Zhang Y, Sun Z (2017) Lithium carbonate recovery from cathode scrap of spent lithium-ion battery: a closed-loop process. *Environ Sci Technol* 51(3):1662–1669. <https://doi.org/10.1021/acs.est.6b03320>
- [2] Kobayashi T, Kobayashi Y, Miyashiro H (2017) Lithium migration between blended cathodes of a lithium-ion battery. *J Mater Chem A* 5:8653–8661. <https://doi.org/10.1039/c7ta02056b>
- [3] Mukai K, Nakano H (2014) Factors affecting the volumetric energy density of lithium-ion battery materials: particle density measurements and cross-sectional observations of layered $\text{LiCo}_{1-x}\text{Ni}_x\text{O}_2$. *ACS Appl Mater Interfaces* 6(13):10583–10592. <https://doi.org/10.1021/am502242z>
- [4] Zhang J, Yao X, Misra RK, Cai Q, Zhao Y (2020) Progress in electrolytes for beyond-lithium-ion batteries. *J Mater Sci Technol* 44:237–257. <https://doi.org/10.1016/j.jmst.2020.01.017>
- [5] Hess M, Lebraud E, Levasseur A (1997) Graphite multilayer thin films: a new anode material for Li-ion microbatteries synthesis and characterization. *J Power Sources* 68(2):204–207. [https://doi.org/10.1016/s0378-7753\(96\)02553-0](https://doi.org/10.1016/s0378-7753(96)02553-0)
- [6] Li T, Cao YL, Ai XP, Yang HX (2008) Cycleable graphite/ FeSi_6 alloy composite as a high capacity anode material for Li-ion batteries. *J Power Sources* 184(2):473–476. <https://doi.org/10.1016/j.jpowsour.2008.02.057>
- [7] Zhao Y, Manthiram A (2015) Amorphous Sb_2S_3 embedded in graphite: a high-rate, long-life anode material for sodium-ion batteries. *Chem Commun* 51:13205–13208. <https://doi.org/10.1039/C5CC03825A>
- [8] Yao WL, Wang JL, Yang J, Du GD (2008) Novel carbon nanofiber-cobalt oxide composites for lithium storage with large capacity and high reversibility. *J Power Sources*

- 176(1):369–372. <https://doi.org/10.1016/j.jpowsour.2007.10.073>
- [9] Zhang L, Zheng S, Wang L, Tang H, Xue H, Wang G, Pang H (2017) Fabrication of metal molybdate micro/nanomaterials for electrochemical energy storage. *Small* 13(33):1700917. <https://doi.org/10.1002/sml.201700917>
- [10] Wang Y, Wu Y, Xing L, Wang Q, Xue X-Y (2016) CoMoO₄/Fe₂O₃ core-shell nanorods with high lithium-storage performance as the anode of lithium-ion battery. *J Alloys Compd* 689:655–661. <https://doi.org/10.1016/j.jallcom.2016.08.023>
- [11] Yang T, Zhang H, Luo Y, Mei L, Guo D, Li Q, Wang T, (2015) Enhanced electrochemical performance of CoMoO₄ nanorods/reduced graphene oxide as anode material for lithium-ion batteries. *Electrochim Acta* 158:327–332. <https://doi.org/10.1016/j.electacta.2015.01.154>
- [12] Ju Z, Zhang E, Zhao Y, Xing Z, Zhuang Q, Qiang Y, Qian Y (2015) One-pot hydrothermal synthesis of FeMoO₄ nanocubes as an anode material for lithium-ion batteries with excellent electrochemical performance. *Small* 11(36):4753–4761. <https://doi.org/10.1002/sml.201501294>
- [13] Feng X, Huang Y, Chen M, Chen X, Li C, Zhou S, Gao X (2018) Self-assembly of 3D hierarchical MnMoO₄/NiWO₄ microspheres for high-performance supercapacitor. *J Alloys Compd* 763:801–807. <https://doi.org/10.1016/j.jallcom.2018.06.025>
- [14] Veerasubramani GK, Krishnamoorthy K, Sivaprakasam R, Kim SJ (2014) Sonochemical synthesis, characterization, and electrochemical properties of MnMoO₄ nanorods for supercapacitor applications. *Mater Chem Phys* 147(3):836–842. <https://doi.org/10.1016/j.matchemphys.2014.06.028>
- [15] Wei H, Yang J, Zhang Y, Qian Y, Geng H (2018) Rational synthesis of graphene-encapsulated uniform MnMoO₄ hollow spheres as long-life and high-rate anodes for lithium-ion batteries. *J Colloid Interface Sci* 524:256–262. <https://doi.org/10.1016/j.jcis.2018.03.100>
- [16] Ezeigwe ER, Khiew PS, Siong CW, Kong I, Tan MTT (2017) Synthesis of NiMoO₄ nanorods on graphene and superior electrochemical performance of the resulting ternary based composites. *Ceram Int* 43(16):13772–13780. <https://doi.org/10.1016/j.ceramint.2017.07.092>
- [17] Seevakan K, Manikandan A, Devendran P, Shameem A, Alagesan T (2018) Microwave combustion synthesis, magneto-optical and electrochemical properties of NiMoO₄ nanoparticles for supercapacitor application. *Ceram Int* 44(12):13879–13887. <https://doi.org/10.1016/j.ceramint.2018.04.235>
- [18] Fei J, Sun Q, Cui Y, Li J, Huang J (2017) Sodium carboxyl methyl cellulose and polyacrylic acid binder with enhanced electrochemical properties for ZnMoO₄·0.8H₂O anode in lithium ion batteries. *J Electroanal Chem* 804:158–164. <https://doi.org/10.1016/j.jelechem.2017.09.061>
- [19] Wan L, Shen J, Zhang Y, Li X (2017) Novel ZnMoO₄/reduced graphene oxide hybrid as a high-performance anode material for lithium ion batteries. *J Alloys Compd* 708:713–721. <https://doi.org/10.1016/j.jallcom.2017.03.078>
- [20] Leyzerovich NN, Bramnik KG, Buhmester T, Ehrenberg H, Fuess H (2004) Electrochemical intercalation of lithium in ternary metal molybdates MMoO₄ (M: Cu, Zn, Ni and Fe). *J Power Sources* 127(1):76–84. <https://doi.org/10.1016/j.jpowsour.2003.09.010>
- [21] Yuan S, Zhu Y-H, Li W, Wang S, Xu D, Li L, Zhang Y, Zhang X-B (2017) Surfactant-Free Aqueous Synthesis of Pure Single-Crystalline SnSe Nanosheet Clusters as Anode for High Energy- and Power-Density Sodium-Ion Batteries. *Adv Mater* 29(4):1602469. <https://doi.org/10.1002/adma.201602469>
- [22] Zhao Y, Peng L, Liu B, Yu G (2014) Single-crystalline LiFePO₄ nanosheets for high-rate li-ion batteries. *Nano Lett* 14(5):2849–2853. <https://doi.org/10.1021/nl5008568>
- [23] Chen Z-h, Huang K-l, Liu S-q, Wang H-y (2010) Preparation and characterization of spinel LiMn₂O₄ nanorods as lithium-ion battery cathodes. *Trans Nonferrous Met Soc China* 20(12):2309–2313. [https://doi.org/10.1016/S1003-6326\(10\)60646-2](https://doi.org/10.1016/S1003-6326(10)60646-2)
- [24] Gong Y, Sun L, Si H, Zhang Y, Shi Y, Wu L, Gu J, Zhang Y (2020) MnO nanorods coated by Co-decorated N-doped carbon as anodes for high performance lithium ion batteries. *Appl Surf Sci* 504:144479. <https://doi.org/10.1016/j.apsusc.2019.144479>
- [25] Su W, Liang Y, Tang Y (2019) Facile situ synthesis of C@SnO₂/Sn@rGO hybrid nanosheets as high performance anode materials for lithium-ion batteries. *J Alloys Compd* 801:402–408. <https://doi.org/10.1016/j.jallcom.2019.05.288>
- [26] Fei J, Sun Q, Li J, Cui Y, Huang J, Hui W, Hu H (2017) Synthesis and electrochemical performance of α-ZnMoO₄ nanoparticles as anode material for lithium ion batteries. *Mater Lett* 198:4–7. <https://doi.org/10.1016/j.matlet.2017.03.160>
- [27] Burton AW, Ong K, Rea T, Chan IY (2009) On the estimation of average crystallite size of zeolites from the Scherrer equation: a critical evaluation of its application to zeolites with one-dimensional pore systems. *Microporous Mesoporous Mater* 117(1):75–90. <https://doi.org/10.1016/j.micromeso.2008.06.010>
- [28] Dreger H, Haselrieder W, Kwade A (2019) Influence of dispersing by extrusion and calendaring on the performance of lithium-ion battery electrodes. *J Energy Storage* 21:231–240. <https://doi.org/10.1016/j.est.2018.11.028>

- [29] Nadimicherla R, Zha R, Wei L, Guo X (2016) Single crystalline flowerlike α - MoO_3 nanorods and their application as anode material for lithium-ion batteries. *J Alloys Compd* 687:79–86. <https://doi.org/10.1016/j.jallcom.2016.06.099>
- [30] Xue R, Hong W, Pan Z, Jin W, Zhao H, Song Y, Zhou J, Liu Y (2016) Enhanced electrochemical performance of ZnMoO_4 /reduced graphene oxide composites as anode materials for lithium-ion batteries. *Electrochim Acta* 222:838–844. <https://doi.org/10.1016/j.electacta.2016.11.045>
- [31] Zhang K, Xu R, Wei R, Li Y, Wang Y, Zhang Y, Dai Y, Yao Y (2020) Tunable polymorph and morphology synthesis of iron oxalate nanoparticles as anode materials for lithium ion batteries. *Mater Chem Phys* 243(1):122676. <https://doi.org/10.1016/j.matchemphys.2020.122676>
- [32] Wang L, Liang W, He S, Liu M, Zhao Y, Zhang W, Chen Y, Lai X, Bi J, Gao D (2020) Realization of superior electrochemical performances for ZnMoO_4 anode material through the construction strategy of 3D flower-like single crystalline. *J Alloys Compd* 816:152673. <https://doi.org/10.1016/j.jallcom.2019.152673>
- [33] Yadav P, Sinha E (2019) Structural, photophysical and microwave dielectric properties of α - ZnMoO_4 phosphor. *J Alloys Compd* 795:446–452. <https://doi.org/10.1016/j.jallcom.2019.05.019>
- [34] Xie Q, Lin L, Ma Y, Zeng D, Yang J, Huang J, Wang L, Peng D-L (2017) Synthesis of ZnO - Cu - C yolk-shell hybrid microspheres with enhanced electrochemical properties for lithium ion battery anodes. *Electrochim Acta* 226:79–88. <https://doi.org/10.1016/j.electacta.2016.12.187>
- [35] Palanisamy K, Kim Y, Kim H, Kim JM, Yoon W-S (2015) Self-assembled porous MoO_2 /graphene microspheres towards high performance anodes for lithium ion batteries. *J Power Sources* 275:351–361. <https://doi.org/10.1016/j.jpowsour.2014.11.001>
- [36] Jiang R, Cui C, Ma H, Ma H, Chen T (2015) Study on the enhanced electrochemical performance of LiMn_2O_4 cathode material at 55°C by the nano Ag-coating. *J Electroanal Chem* 744:69–76. <https://doi.org/10.1016/j.jelechem.2015.02.016>
- [37] Wang Y, Xing G, Han ZJ, Shi Y, Wong JI, Huang ZX, Ostrikov K, Yang HY (2014) Pre-lithiation of onion-like carbon/ MoS_2 nano-urchin anodes for high-performance rechargeable lithium ion batteries. *Nanoscale* 6(15):8884–8890. <https://doi.org/10.1039/C4NR01553C>
- [38] Wang H-Q, Lai F-Y, Li Y, Zhang X-H, Huang Y-G, Hu S-J, Li Q-Y (2015) Excellent stability of spinel LiMn_2O_4 -based cathode materials for lithium-ion batteries. *Electrochim Acta* 177:290–297. <https://doi.org/10.1016/j.electacta.2015.02.027>
- [39] Yu Y, Xiang M, Guo J, Su C, Liu X, Bai H, Bai W, Duan K (2019) Enhancing high-rate and elevated-temperature properties of Ni-Mg co-doped LiMn_2O_4 cathodes for Li-ion batteries. *J Colloid Interface Sci* 555:64–71. <https://doi.org/10.1016/j.jcis.2019.07.078>
- [40] Wang F-M, Rick J (2014) Synergy of Nyquist and Bode electrochemical impedance spectroscopy studies to commercial type lithium ion batteries. *Solid State Ionics* 268(15):31–34. <https://doi.org/10.1016/j.ssi.2014.09.023>
- [41] Wang F-M, Cheng H-M, Wu H-C, Chu S-Y, Cheng C-S, Yang C-R (2009) Novel SEI formation of maleimide-based additives and its improvement of capability and cyclicability in lithium ion batteries. *Electrochim Acta* 54(12):3344–3351. <https://doi.org/10.1016/j.electacta.2008.12.032>
- [42] Shimizu M, Yatsuzuka R, Koya T, Yamakami T, Arai S (2018) Tin oxides as a negative electrode material for potassium-ion batteries. *ACS Appl Energy Mater* 1(12):6865–6870. <https://doi.org/10.1021/acsaeam.8b01209>

Publisher's Note Springer Nature remains neutral with regard to jurisdictional claims in published maps and institutional affiliations.